

Evolution of temperature profiles in TiNi films for elastocaloric cooling

H. Ossmer^{a,*}, F. Lambrecht^a, M. Gültig^a, C. Chluba^b, E. Quandt^b, M. Kohl^a

^a Karlsruhe Institute of Technology, IMT, PO Box 3640, 76021 Karlsruhe, Germany

^b Christian Albrecht University Kiel, Institute for Material Science, 24143 Kiel, Germany

Received 12 June 2014; received in revised form 29 July 2014; accepted 2 August 2014

Available online 6 September 2014

Abstract

The time-resolved strain and temperature profiles of magnetron-sputtered pseudoelastic TiNi films of 20 μm thickness are investigated during tensile stress cycling for different strain rates. Based on simultaneous infrared thermography and digital image correlation, a good correlation between the evolution of temperature profiles and the local formation and propagation of Lüders-like strain bands is observed. The evolution of temperature profiles can be quantitatively described by a phenomenological Tanaka-type model of the martensitic transformation combined with a heat transfer model taking into account the local interaction between transformed and untransformed regions in the transformation kinetics. The investigated film samples exhibit an undercooling of -16 K upon mechanical unloading under adiabatic conditions at a strain rate of 0.2 s^{-1} . A coefficient of performance of 7.7 is determined. Due to the high surface-to-volume ratio, the films show fast heat exchange in air of the order of 1.5 s. Based on these results, the prospects of SMA film-based elastocaloric cooling are discussed.

© 2014 Acta Materialia Inc. Published by Elsevier Ltd. All rights reserved.

Keywords: Elastocaloric effect; Ti–Ni; Film; Local strain distribution; Shape memory alloy (SMA)

1. Introduction

Solid-state cooling has been recognized as a promising alternative to conventional vapor-compression cooling technology due to its potential to save energy and minimize greenhouse gas emission in macroscopic applications as well as due to its potential for down-scaling, which enables novel routes for microcooling. Depending on the kind of applied field (magnetic field, electric field, pressure, stress), different caloric effects may be distinguished [1–3]. Analogies between the caloric effects can be collectively described by the influence of the applied fields and corresponding generalized displacements on entropy [4]. Since the end of the 1990s, the magnetocaloric effect has received considerable attention due to the first demonstration of a proof-of-principle magnetic refrigerator [5] and the discovery of the

giant magnetocaloric effect in $\text{Gd}_5(\text{Si}_2\text{Ge}_2)$ [6]. Recently, giant electrocaloric effects have also been reported in PZT films near the ferroelectric Curie temperature [7]. Shape memory alloys (SMAs) are good candidates to show baro- and elastocaloric effects as they undergo a diffusionless stress-induced first-order phase transformation [8], which is an important condition for large entropy changes to occur [9].

The elastocaloric effect may be induced by applying uniaxial stress at a temperature above the austenite finish temperature A_f causing the formation of oriented martensite. The stress-induced martensite (SIM) transformation is exothermic. When relieving a stressed sample from the SIM state after temperature equalization with the environment, the endothermic reverse transformation takes place, resulting in an undercooling below ambient temperature. This elastocaloric effect in SMAs appears to be particularly promising for cooling applications as the stress required to induce a temperature change can be tuned over a large

* Corresponding author.

E-mail address: hinnerk.ossmer@kit.edu (H. Ossmer).

range, while large external electrical or magnetic fields are avoided. The theoretical maximum temperature change that can be obtained under adiabatic conditions depends only on the latent heat of the transformation and the material's heat capacity. Maximum values of the adiabatic temperature change reported for the elastocaloric effect in TiNi exceed the typical values found for the other ferroic-caloric effects [1]. Investigations on TiNi wires, for instance, reveal a temperature increase of 25.5 K upon loading and of 17 K upon unloading [10].

However, due to the rather large dimensions of the investigated specimens, heat transfer times are well above 10 s. Considerable improvements are expected for film specimens with high surface-to-volume ratio, enabling faster heat transfer times and thus higher cycling frequencies. Therefore, it is advantageous to combine many SMA films to form distributed film arrays instead of using a single bulk specimen for elastocaloric cooling. Recent investigations of TiNi-based films have concentrated on effect size and functional fatigue [11]. For the development of a film device under real operational conditions it is essential to understand and tailor the evolution of temperature profiles during cyclic loading and unloading.

In this paper, we present an analysis of time-resolved strain and temperature profiles in magnetron-sputtered TiNi films during stress cycling in order to evaluate the time and spatial dependence of the elastocaloric effect down to the length scale of 25 μm . A phenomenological model is presented to account for the experimental results.

2. Experimental

All the experiments described in the present work are conducted on $\text{Ni}_{50.4}\text{Ti}_{49.6}$ films 20 μm thick. The films are deposited by DC magnetron sputtering onto a glass substrate with pre-structured sacrificial copper layer at a power of 300 W and Ar flow rate of 20 sccm at 2×10^{-3} mbar during sputter deposition. The base pressure is 10^{-7} mbar. The deposition rate is 3.8 nm s^{-1} . Since the as-deposited films are amorphous, a heat-treatment procedure is established that comprises a two-step rapid thermal annealing at 650 $^{\circ}\text{C}$ for 10 min and at 450 $^{\circ}\text{C}$ for 10 min. For tensile tests, the films are structured in stripes 1.75 mm wide and 35 mm long. Details of the fabrication and structuring process can be found in Ref. [11].

The physical properties of the polycrystalline samples investigated within this work depend on the load history. During the first 20 tensile loading and unloading cycles, the pseudoelastic performance of investigated samples undergoes characteristic changes due to training and fatigue before stabilizing [12]. In the following, the results are presented from as-received samples to obtain material parameters such as critical stress and the elastic moduli and to study the mechanisms of phase transformation on the mesoscale. In addition, results are presented from samples that have been subjected to at least 20 training cycles, which are more relevant for elastocaloric cooling

applications requiring stable material behavior under cyclic loading.

The phase transformation temperatures, latent heat and heat capacity are determined by differential scanning calorimetry (DSC). Additional temperature-dependent electrical resistance measurements are performed to study the course of phase transformation. DSC measurements are conducted under nitrogen inert gas flow of 10 ml s^{-1} with a heating rate of 10 K min^{-1} . Electrical four-wire measurements are performed in a thermostat under vacuum of $\sim 2 \times 10^{-2}$ mbar. Quasi-static conditions are maintained by waiting for stationary measurement signals before data acquisition. The specific heat capacity c_p is determined by DSC at a heating rate of 20 K min^{-1} employing a synthetic sapphire standard.

A schematic of the tensile test setup is shown in Fig. 1. The tensile testing machine is equipped with a 50 N force sensor. Uniaxial tensile loads are applied at room temperature in air. The resolutions of the force and distance measurements are 0.25 N and 0.25 μm , respectively. Samples are attached to small glass or ceramic plates with a two-component adhesive, and these plates are then clamped to the machine by screws. Thus, stress peaks at the sample ends are minimized and thermal insulation is improved. Engineering strains are determined from the cross-beam position $L(t)$ of the tensile testing machine and the initial sample length L_0 according to $\varepsilon = (L(t) - L_0)/L_0$. Cyclic tensile tests are performed in strain-control mode with different strain rates between 10^{-4} and 20 s^{-1} . In order to avoid buckling of the sample a tensile pre-load of 1 N is applied before load cycling. After loading and unloading, the sample is held in a static position to allow for thermal equilibration with the environment.

During tensile tests, samples are monitored with an infrared camera and a CCD camera equipped with a microscope lens. Samples are covered with a thin layer of graphite spray on both sides to improve thermal emissivity. Thermal images are acquired with a frame rate of up to 100 Hz and a spatial resolution of 25 μm . In experiments with slow strain rates, close-up images in the visible range are acquired with a frame rate of 10 Hz. The obtained micrographs are used to calculate local strain profiles by the digital image correlation (DIC) technique [13].

3. Thermomechanical model

A number of theoretical models have been developed in order to describe the pseudoelastic behavior of SMA materials — for a recent review see, for example, Refs. [14,15]. In particular, for engineering of pseudoelastic SMA components, different descriptions for the kinematics of the phase transformation and different approaches to the development of the free energy and dissipation have been developed and implemented in a finite-element (FEM) program [16–19]. Up to now, only a few FEM studies on SMAs reflect localized deformation [20,21]. In this work, we built on a two-phase phenomenological model that was originally for-

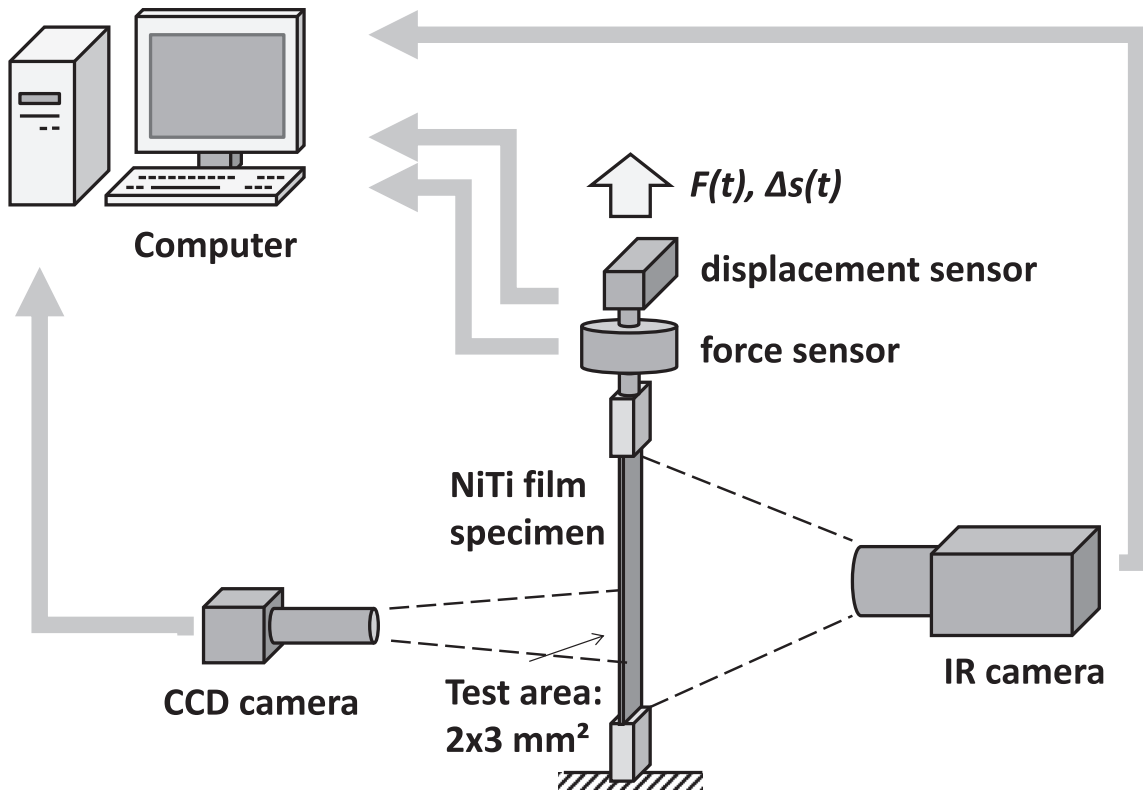


Fig. 1. Schematic of tensile test setup for measurement of global as well as mesoscale mechanical and thermal properties. Local temperature profiles are determined by an infrared camera. Local strain fields are calculated by digital image correlation from optical micrographs.

ulated by Tanaka [22] and further developed in Refs. [23–25]. In this model, the martensite phase fraction ξ is introduced as an internal variable that depends on the evolution of temperature and stress. The model relies on the material parameters and experimentally accessible fit parameters of the TiNi films under investigation.

Two separate equations are employed to describe the martensitic phase fraction ξ during forward and reverse transformation in order to reproduce hysteretic material behavior:

$$\xi^{AM}(T, \sigma^*) = f(k^{AM} \cdot [T - T_0^{AM} - c^{AM} \cdot \sigma^*]), \quad (1a)$$

$$\xi^{MA}(T, \sigma^*) = f(k^{MA} \cdot [T - T_0^{MA} - c^{MA} \cdot \sigma^*]). \quad (1b)$$

The temperatures T_0^{AM} and T_0^{MA} are the peak temperatures of the martensitic and reverse transformation, respectively. The effective local stress σ^* is determined using the Tresca stress. The parameters $c^{AM} = [d\sigma_c^{AM}/dT]^{-1}$ and $c^{MA} = [d\sigma_c^{MA}/dT]^{-1}$ describe the linear stress–temperature dependence according to the Clausius–Clapeyron relationship for forward and reverse transformation, respectively. The width of the transformation corresponding to the inclination of the pseudoelastic stress plateau is described by the fit parameters k^{AM} and k^{MA} . The function $f(x)$ represents a soft step function. In previous work, exponential functions have been used that reproduce experimental transformation characteristics with reasonable accuracy [24]. Here, we use the antiderivative of the Gaussian bell

curve in order to simplify the formulation of the partial differential equation for the time-evolution of the phase fraction:

$$\frac{d\xi}{dt} = \frac{\partial \xi}{\partial \sigma^*} \cdot \frac{d\sigma^*}{dt} + \frac{\partial \xi}{\partial T} \cdot \frac{dT}{dt}. \quad (2)$$

In Section 6, possible extensions of Eq. (2) will be discussed to implement local interactions between transformed and untransformed regions.

The martensite and austenite phase are assumed to be mechanically connected in parallel in each volume element. Therefore, the mechanical stresses in both phases contribute to the total stress:

$$\sigma = (1 - \xi) \cdot E_A \cdot \varepsilon + \xi \cdot E_M \cdot (\varepsilon - \varepsilon_T), \quad (3)$$

where E_A and E_M are the Young's moduli of austenite and martensite phase, respectively. ε denotes the absolute value of local strain and ε_T the maximum transformation strain due to orientation of martensite variants in the loading direction.

In order to account for temperature changes related to the release and absorption of latent heat, a volume heat source Q_L is introduced that depends on the time-dependent change of phase fraction $\dot{\xi}$:

$$Q_L(T, \sigma^*) = L \cdot \rho \cdot \dot{\xi}(T, \sigma^*), \quad (4)$$

where L is the mass specific latent heat, and ρ the mass density. Assuming isotropic thermal properties, the heat transfer is described by the differential equation:

$$\rho \cdot C_p \cdot \dot{T} + \rho \cdot C_p \cdot \vec{u} \cdot \Delta T = \nabla \cdot (\lambda \cdot \nabla T) + Q_L + Q_C, \quad (5)$$

which takes into account the sensible heat, the advection, the heat of phase transformation and losses due to heat conduction. The parameters m , C_p and λ denote the mass, specific heat capacity and thermal conductivity, respectively. At the film surface, the boundary condition is considered:

$$-\vec{n} \cdot (-\lambda \nabla T) = K \cdot (T_E - T), \quad (6)$$

which takes the convective heat exchange with the environment of temperature T_E into account. The parameter K denotes the heat transfer coefficient. The thermal boundaries at the sample fixation are considered to be isothermal, and are therefore held constant at T_E .

The mechanical and thermal equations are solved by coupled FEM analysis using the software tool COMSOL Multiphysics.

The material parameters used for the simulation are summarized in Table 1. The elastic moduli of austenite and martensite E_A and E_M as well as the transformation strain ε_T are obtained from linear least-squares fit of the stress–strain characteristics determined under quasi-static experimental conditions. The Clausius–Clapeyron coefficient $c^{AM} = [d\sigma_c^{AM}/dT]^{-1}$ is determined based on the critical stress σ_c^{AM} in the center of the martensitic stress plateau at two different ambient temperatures T_E . Using the value of 8.75 MPa K^{-1} for the Clausius–Clapeyron coefficient in our simulations shows the best agreement with the strain rate-dependent change of stress in our stress–strain experiments. In particular, the respective coefficient of reverse transformation is assumed to be identical, because we observe a similar change of stress due to self-heating upon loading and self-cooling upon unloading when increasing the strain rate. The phase transformation temperatures T_0^{AM} and T_0^{MA} are calculated by inserting the critical stress values in Eqs. (1a) and (1b) using the condition $f(0) = 0.5$. The corresponding parameter sets describe the center of the stress plateaus, where the martensitic phase fraction is 0.5 according to the present model. Finally, the parameters k^{AM} and k^{MA} are adapted to adjust

the inclination of the plateaus to the experimental characteristics.

4. Phase transformation properties

Fig. 2 shows the temperature-dependent electrical resistance and DSC measurements under quasi-static conditions. The material exhibits a two-stage phase transformation from austenite to martensite via an intermediate R-phase. Upon cooling, the electrical resistance measurement exhibits the characteristic anomaly of a two-stage transformation showing an increase due to R-phase transformation followed by a decrease due to martensitic transformation. Upon heating, the corresponding reverse transformations occur. Correlating this observation with the DSC results allows the small peak in the inset to be interpreted as transformation from martensite to intermediate R-phase. The austenite finish temperature A_f is $\sim 20^\circ\text{C}$, which is important to achieve pseudoelastic behavior at room temperature. The specific heat capacity c_p is determined in a temperature regime well above the first-order phase transformation between 110 and 150°C according to the ASTM standard E1269 [26] to be $0.45 \text{ J g}^{-1} \text{ K}^{-1}$. The c_p of the martensite state is assumed to be the same, which is in line with our DSC results shown in Fig. 2. The measured latent heat of the complete two-stage transformation is $\sim 20 \text{ J g}^{-1}$. However, the latent heat accessible in the tensile test experiments is smaller as will be discussed below.

5. Pseudoelastic performance

A typical engineering stress–strain characteristic is shown in Fig. 3 for an as-received sample determined at a low strain rate of 10^{-4} s^{-1} . Pronounced stress plateaus are observed during forward and reverse martensitic transformation. SIM transformation starts at a critical strain of $\sim 1.3\%$ and proceeds at an almost constant stress level of 500 MPa. During unloading, the plateau of the reverse transformation locates at a lower stress level between 350

Table 1
Simulation parameters for thermomechanical FEM simulation of TiNi tensile test specimens.

Parameter	Value	Source
T_0^{MA}, T_0^{AM}	268.9 K, 249.2 K	Derived from tensile test
k^{MA}, k^{AM}	0.45 K^{-1} , 0.45 K^{-1}	Derived from tensile test
$d\sigma_c^{MA}/dT, d\sigma_c^{AM}/dT$	8.75 MPa K^{-1} , 8.75 MPa K^{-1}	Tensile test at various T
L	7.2 J g^{-1}	Estimation based on experiment
ε_T	0.035	Tensile test
E_A, E_M	30 GPa, 22 GPa	Tensile test
λ	$0.18 \text{ W cm}^{-1} \text{ K}^{-1}$	Literature (austenite)
K	$18 \text{ W m}^{-2} \text{ K}^{-1}$	Estimation
Sample length, width, thickness	15 mm, 2 mm, 20 μm	
ν (Poisson's ratio)	0.3	Literature
ρ (mass density)	6500 kg m^{-3}	Literature
C_p	$450 \text{ J kg}^{-1} \text{ K}^{-1}$	DSC measurement

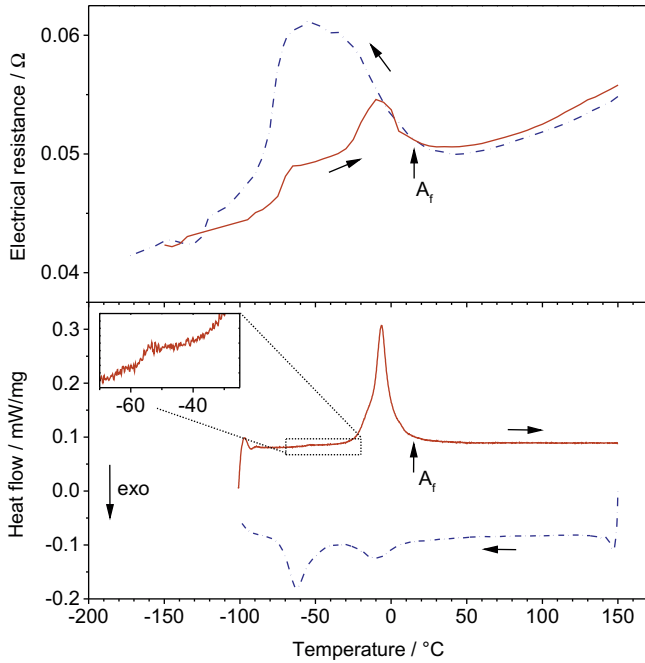


Fig. 2. (a) Electrical resistance and (b) differential scanning calorimetry measurement for a heating rate of 10 K min^{-1} in the temperature range of phase transformation. The austenite finish temperature is indicated.

and 400 MPa. Fig. 3 includes a simulation characteristic based on the phenomenological model outlined in Section 3 for the simulation parameters given in Table 1. The simulation describes the experimental stress–strain behavior quite accurately. Deviations occur mostly at high strain, where the martensitic phase fraction approaches 1.

Due to the quasi-static conditions realized at small strain rates, the sample thermally equilibrates with the ambient. Hence, the sample temperature stays approximately constant during martensitic and reverse transformation. With increasing strain rate, however, self-heating and self-cooling occurs during loading and unloading, respectively, affecting the pseudoelastic performance. In particular, the increase of temperature during forward transformation hampers the phase transformation,

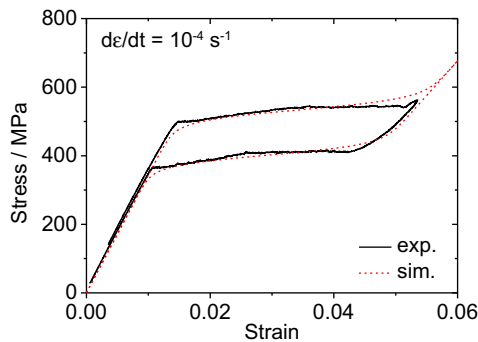


Fig. 3. Experimental stress–strain characteristic of an as-received TiNi film sample under quasi-static conditions (black curve). A corresponding simulation characteristic is shown by the red dashed line. (For interpretation of the references to color in this figure legend, the reader is referred to the web version of this article.)

resulting in an increasing slope of the pseudoelastic plateau. Similarly, the reverse transformation is hampered by undercooling during unloading. Both effects have been described in previous work (e.g. [27]).

These effects cause characteristic changes in the mechanical work balance as shown in Fig. 4. The mechanical work per unit volume during loading and unloading, W_{load} and W_{unload} , is determined from the stress–strain characteristics at different strain rates by numerical integration of the loading and unloading trajectories, respectively. Before the experiment, 20 training cycles have been performed at a slow rate to allow for stabilization. The dissipated work is determined by the difference $\Delta W = W_{load} - W_{unload}$. ΔW is strain-rate dependent, starting at 3 J m^{-3} in the quasi-static experiment and increasing up to 7.5 J m^{-3} at a strain rate of 0.2 s^{-1} . At this strain rate, the pseudoelastic material displays its full damping capacity. In previous investigations, a pronounced damping maximum has been observed, if thermal equilibration with the ambient is not allowed between the mechanical loading and unloading step [26,28]. In the present experiment, the sample is given enough time to equilibrate before unloading begins. In this case, damping does not decrease at strain rates above 0.2 s^{-1} when approaching the adiabatic limit.

6. Evolution of temperature profiles

By performing simultaneous infrared thermography and DIC measurements during tensile loading and unloading, temperature and strain profiles are correlated as a function of time. Fig. 5 shows a series of thermograms and corresponding strain maps that have been recorded for increasing strain at low strain rate of 0.02 s^{-1} . These experiments reveal a number of striking features that can be summarized as follows:

- Upon loading, we observe the formation of sharp local strain bands at an angle of 55° with respect to the loading direction. The large strain within the strain bands of 5.3% indicates the presence of oriented martensite. All other regions remain

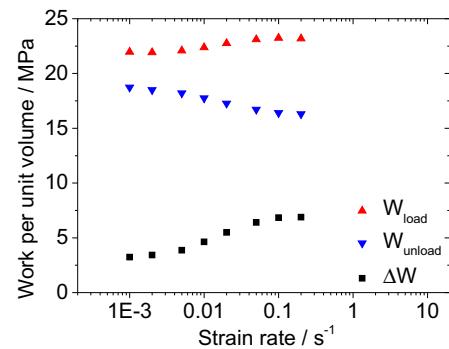


Fig. 4. Strain-rate dependence of mechanical work during loading and unloading as well as corresponding mechanical work balance $\Delta W = W_{load} - W_{unload}$ for a complete loading cycle.

unstrained, indicating that they are still in the austenitic condition. The formation of strain bands and corresponding phase boundaries is correlated with the formation of temperature bands at elevated temperature.

- (b) Strain bands and temperature bands form at the sample edges near the sample fixation. Depending on the boundary conditions of the sample fixation, asymmetries in strain and temperature profiles occur between the upper and lower end of the samples.
- (c) The strain bands increase in size by propagation of phase boundaries upon loading. The corresponding temperature bands increase in size as well.
- (d) Temperature maxima propagate towards the center of the sample and broaden in width due to heat transfer to the sample ends and neighboring regions.
- (e) While keeping the sample in the maximum strain state the temperature homogenizes and decreases due to heat transfer. A similar series of experiments is shown in Fig. 6 for decreasing strain after thermal equilibration at maximum strain. In this case, the main observations are:
- (f) During mechanical unloading, bands of zero strain and the corresponding phase boundaries of the reverse transformation first appear at those locations where the martensitic transformation has ended before. At these locations, temperature bands with decreased temperature form.

- (g) The bands of zero strain increase in size due to propagation of phase boundaries during unloading. Corresponding undercooled regions increase in size as well.
- (h) Compared to the loading process, temperature minima propagate in the reverse direction towards the sample ends, where temperature gradients decrease due to heat transfer.

For increasing strain rates, the number of strain bands increases. In addition, temperature changes increase until adiabatic conditions are reached as will be discussed below in Section 7.

In order to understand the observed temperature evolution in the TiNi film samples, a series of finite-element simulations has been performed using the phenomenological model outlined in Section 3 with the simulation parameters given in Table 1. Figs. 7 and 8a show a series of simulated thermograms for a strain rate of 0.02 s^{-1} upon loading and unloading, respectively. The simulation describes the local formation of martensite at the sample edges near the sample mounts, which is in line with the experiment. Due to the boundary conditions of sample fixation, tensile loading causes maximum stress at the sample edges. The preferred phase transformation in these regions gives rise to the local increase of temperature in the initial phase of tensile loading. Martensite formation is further stabilized in the regions at the sample edges

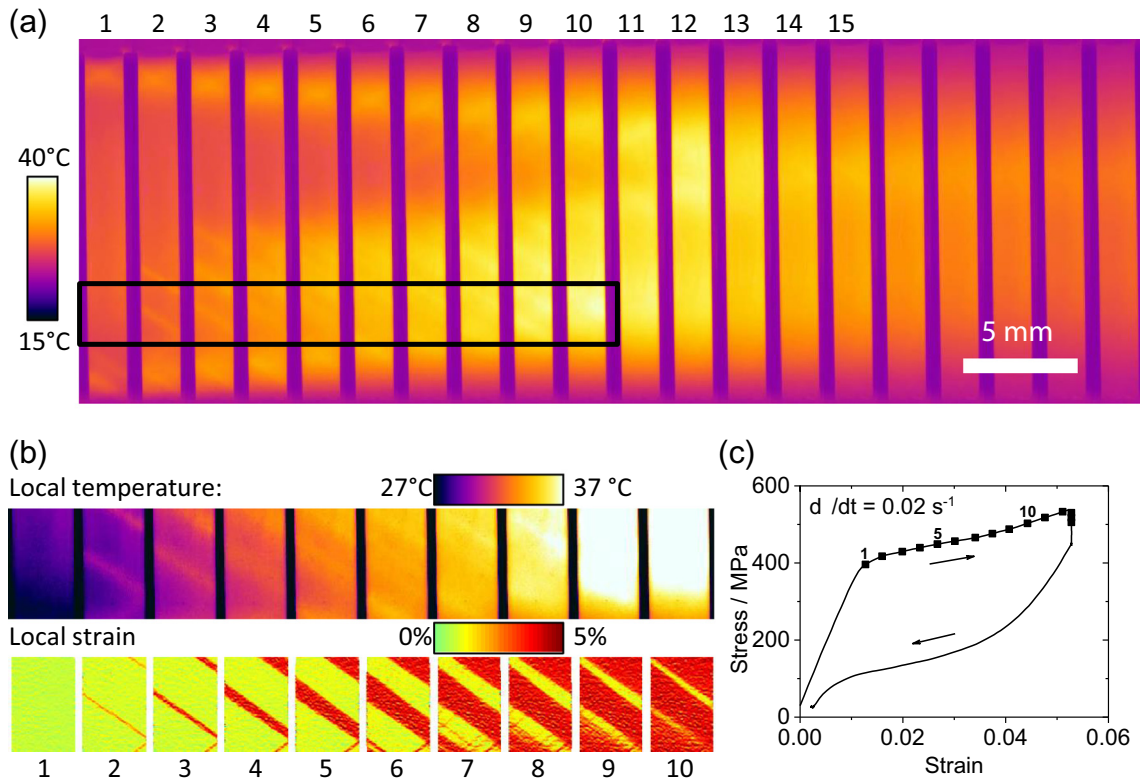


Fig. 5. (a) Series of thermograms of a TiNi film sample during pseudoelastic loading at a strain rate of 0.02 s^{-1} . Images are numbered consecutively. The time interval between two adjacent images is 0.2 s. (b) Profiles of temperature and local strain of a test area in the lower half of the sample as indicated by the box in (a). (c) Stress-strain characteristic including the stress-strain values of image acquisition.

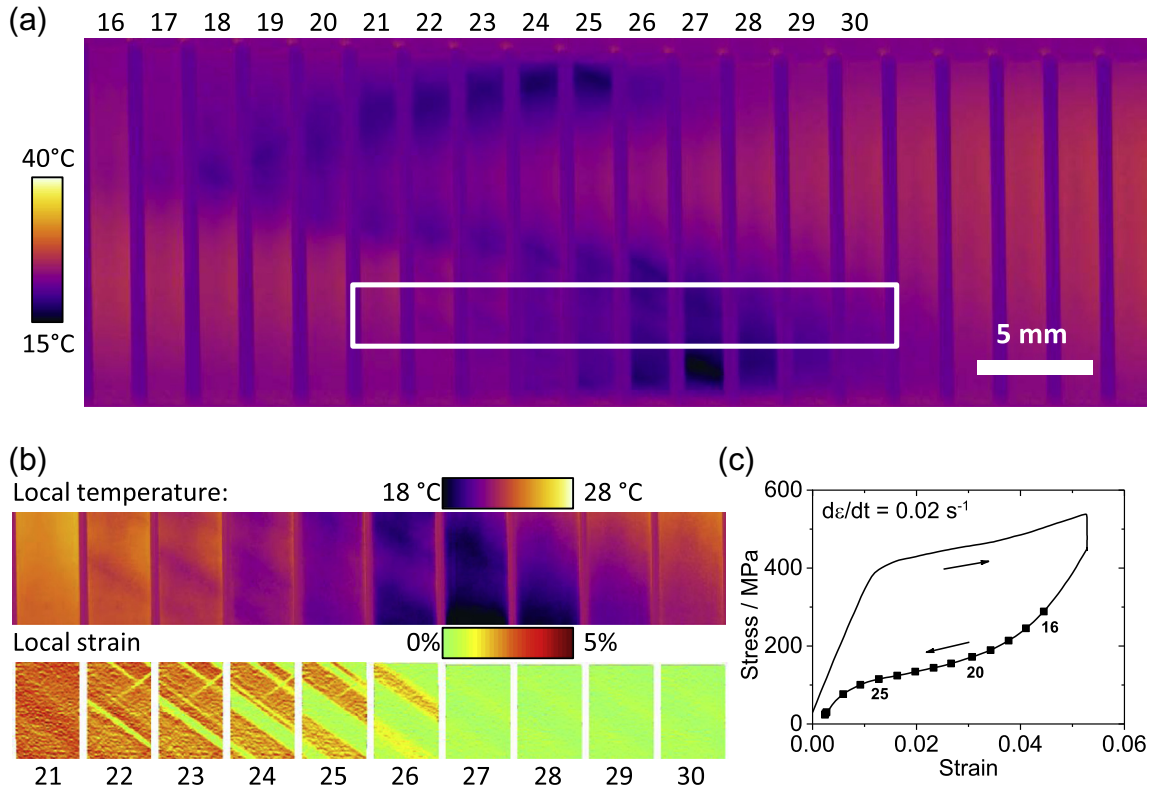


Fig. 6. (a) Series of thermograms of a TiNi film sample during pseudoelastic unloading at a strain rate of 0.02 s^{-1} . Images are numbered consecutively. The time interval between two adjacent images is 0.2 s. (b) Profiles of temperature and local strain of a test area in the lower half of the sample as indicated by the box in (a). (c) Stress–strain characteristic including the stress–strain values of image acquisition.

due to stronger conductive cooling compared to the other regions of the sample.

The simulated regions of martensite formation are on the length scale of discrete finite elements, and thus do not reflect the experimentally observed sharp strain bands. However, this has a minor effect on the evolution of temperature profiles, which broaden as a function of time due to heat transfer. The simulation model captures the heat transfer effects due to heat conduction and convection, causing broadening of the regions of elevated and degraded temperature over time as well as temperature homogenization.

In the center regions of the sample, the simulated temperature evolution deviates from the experiment. Figs. 7 and 8a reveal a homogeneous increase and decrease of temperature as a function of time in the central regions of the sample, while the experiment reveals the propagation of distinct regions of elevated and degraded temperature, respectively. In its present form, the simulation model does not describe the propagation of phase boundaries from the sample edges towards the center upon loading and from the center towards the sample edges upon unloading. In order to include the effect of the propagation of strain bands and related phase boundaries, different approaches have been proposed, including strain gradient effects [19] or additional loading conditions [20], that take the effect of

transformed elements on the mechanical response of adjacent elements into account. Following these lines, we modify the kinetics of phase transformation, Eq. (2), by an additional location-dependent term that favors the increase/decrease of martensite adjacent to an existing phase boundary upon loading/unloading:

$$\frac{d\xi}{dt} = \frac{\partial \xi}{\partial \sigma^*} \cdot \frac{d\sigma^*}{dt} + \frac{\partial \xi}{\partial T} \cdot \frac{dT}{dt} + \beta_{\text{int}} \cdot \frac{d^2 \xi}{dx^2}. \quad (7)$$

Figs. 7 and 8b and c show a series of simulated strain and temperature profiles upon loading and unloading, respectively, using the modified Eq. (7) with $\beta_{\text{int}} = 4 \times 10^{-6}$. The temperature profiles now reveal the evolution of phase transformation fronts close to the stress maxima at the sample edges and their propagation towards the sample center for increasing mechanical load. The phase transformation fronts have gradual boundaries. This gives rise to an additional positive contribution in Eq. (7), resulting in a broadening of the transformed martensitic regions, and thus the propagation of temperature peaks instead of a homogeneous increase of temperature. Similarly, local formation of austenite upon unloading results in an additional negative contribution in Eq. (7), resulting in a broadening of reverse transformed regions and corresponding propagation of regions of minimum temperature. In the model, the sensitivity of the phase fraction ξ on temperature and

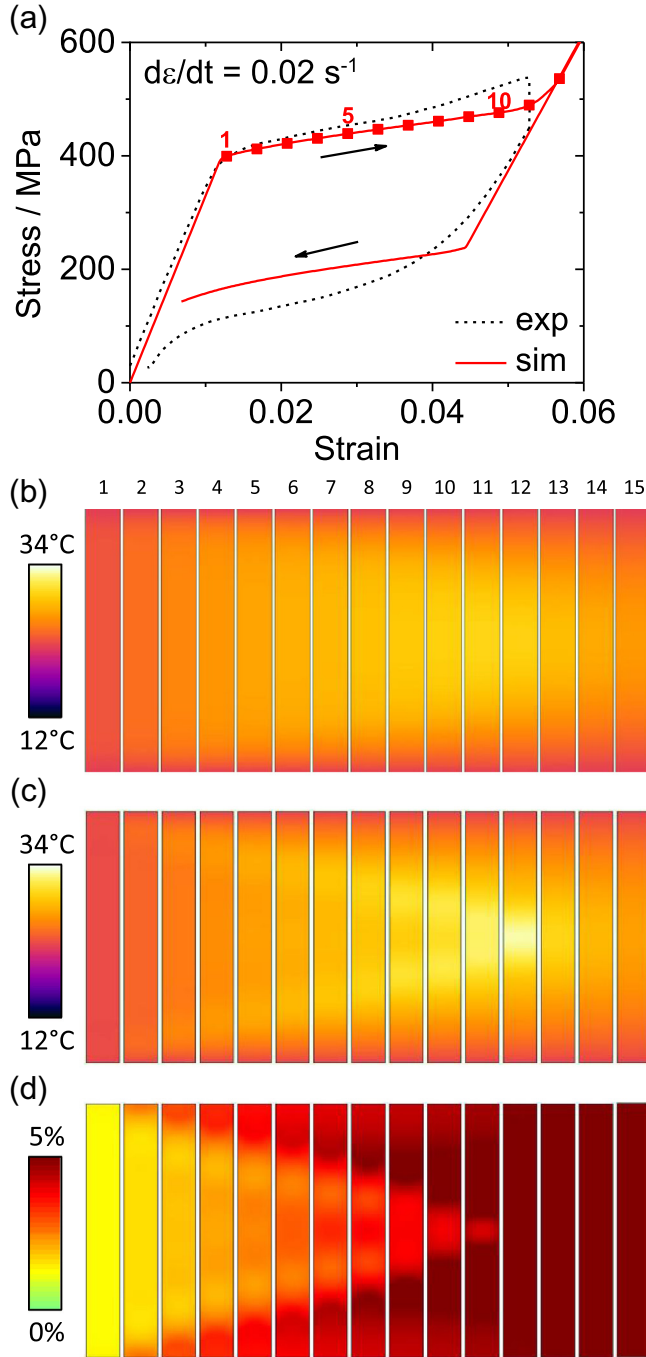


Fig. 7. (a) Experimental and simulated stress–strain characteristic of TiNi film sample during strain-controlled tensile test with $d\varepsilon/dt = 0.02 \text{ s}^{-1}$. Numbered points indicate the values of image acquisition. (b) Corresponding temperature distribution during mechanical unloading, simulated with the original FEM model as described in Section 3. (c) Temperature distribution and (d) local strain field simulated with the extended model. Images are numbered consecutively. The time interval between two adjacent images is 0.2 s.

stress is adjusted by the fit parameters k^{AM} and k^{MA} . An optimum match with experimental results is found when using the values $k^{AM} = k^{MA} = 4.5 \text{ K}^{-1}$, which are larger compared to the original model.

During mechanical unloading, simulated transformation fronts also evolve at the sample edges and propagate

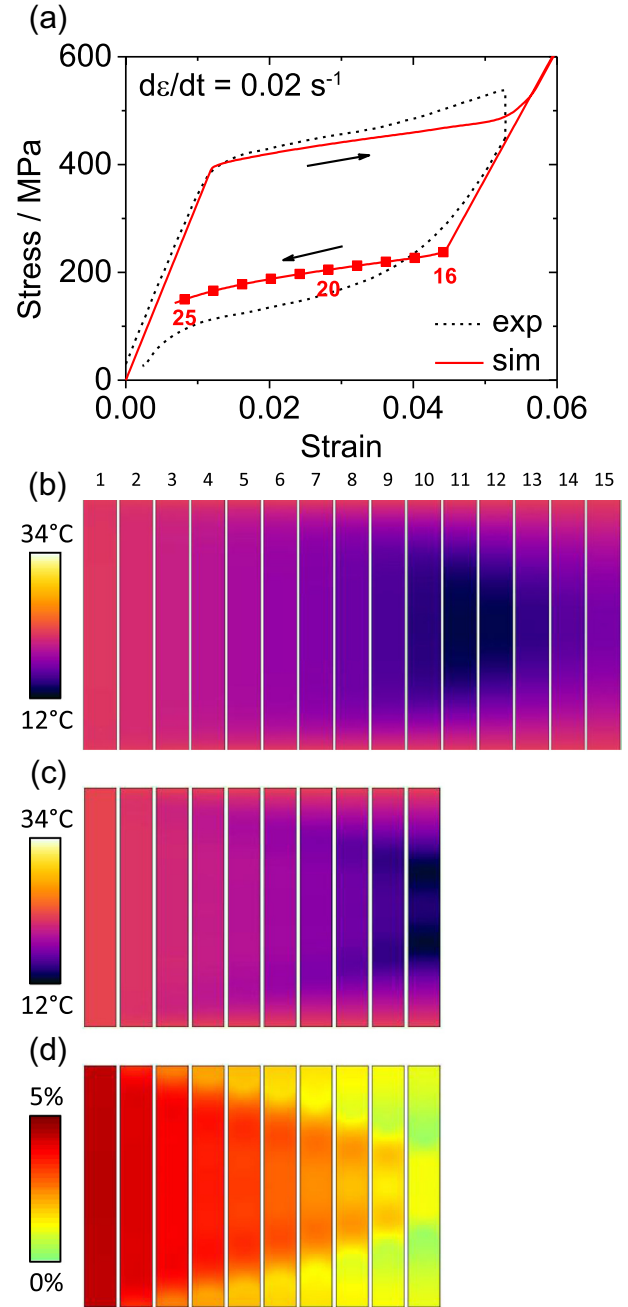


Fig. 8. (a) Experimental and simulated stress–strain characteristic of TiNi film sample during strain-controlled tensile test with $d\varepsilon/dt = 0.02 \text{ s}^{-1}$. Numbered points indicate the values of image acquisition. (b) Corresponding temperature distribution during mechanical unloading, simulated with the original FEM model as described in Section 3. (c) Temperature distribution and (d) local strain field simulated with the extended model. Images are numbered consecutively. The time interval between two adjacent images is 0.2 s.

towards the center. This behavior is experimentally observed, however, only at the lower sample edge. The observed reverse transformation tends to nucleate at those locations where the martensitic transformation had ended before, indicating that phase boundaries are still present at the end of mechanical loading due to incomplete phase transformation. These effects result in an asymmetric

temperature evolution along the sample. In general, nucleation sites may strongly depend on sample inhomogeneity and imperfect thermal and mechanical boundary conditions, which are not considered in the simulation.

7. Evaluation of the elastocaloric cooling effect

For elastocaloric cooling applications, we consider the temperature evolution averaged over a representative area of the sample that might be used for local cooling. In the following, the evolution of maximum and minimum temperature is averaged over an area of 1 mm^2 in the sample center. The effect of strain rate on the temperature change is investigated in the range between 0.001 and 1 s^{-1} . Fig. 9 shows a series of time-resolved characteristics of maximum temperature upon loading and minimum temperature upon unloading for different strain rates. Upon loading, the temperature first remains unchanged while the sample is elastically deformed in the austenite state until the critical stress for martensitic transformation is reached. The temperature rises proportionally to the strain rate and reaches a maximum towards the end of transformation. The maximum temperature is strain-rate dependent due to the heat transfer by heat conduction and convection. For the highest strain rate of 1 s^{-1} , we observe a maximum temperature increase of 17 K . While the sample is kept in a strained condition at 5.3% for 10 s the temperature equilibrates with the ambient. This equilibration process can be well approximated by a single exponential decay with a time constant of $\sim 1.5 \text{ s}$.

Upon unloading, the reverse transformation starts instantly. The temperature decrease is again proportional to the strain rate. In addition, the minimum temperature reached towards the end of reverse transformation depends on the strain rate as well as on heat transfer. The maximum temperature decrease observed for the strain rate of 1 s^{-1} is $\sim -16 \text{ K}$. The time constant determined for the temperature equilibration is about the same for the loading and unloading cases.

The main features of the experimental characteristics are well reproduced by the corresponding simulation characteristics as can be seen in Fig. 9b.

Fig. 10 summarizes the maximum and minimum temperatures observed in Fig. 9. At low strain rates of $2 \times 10^{-3} \text{ s}^{-1}$ and below, temperature changes are low and vanish completely in the quasi-static limit. At high strain rates, on the other hand, the maximum temperature change ΔT saturates in the loading and unloading case at $\Delta T_{\text{load}} = 17 \text{ K}$ and $\Delta T_{\text{unload}} = -16 \text{ K}$, respectively. These results are in line with an estimate of the adiabatic limit according to $\Delta T_{\text{ad}} = L/c_p$ using the specific heat capacity of $0.45 \text{ J g}^{-1} \text{ K}^{-1}$ and a latent heat L of 7.2 J g^{-1} . This value is lower than the latent heat observed for the complete martensitic transformation (Fig. 2), indicating that the sample only undergoes part of the two-stage transformation during load cycling. Assuming a Clausius–Clapeyron coefficient for the investigated films of 8.75 MPa K^{-1} , the

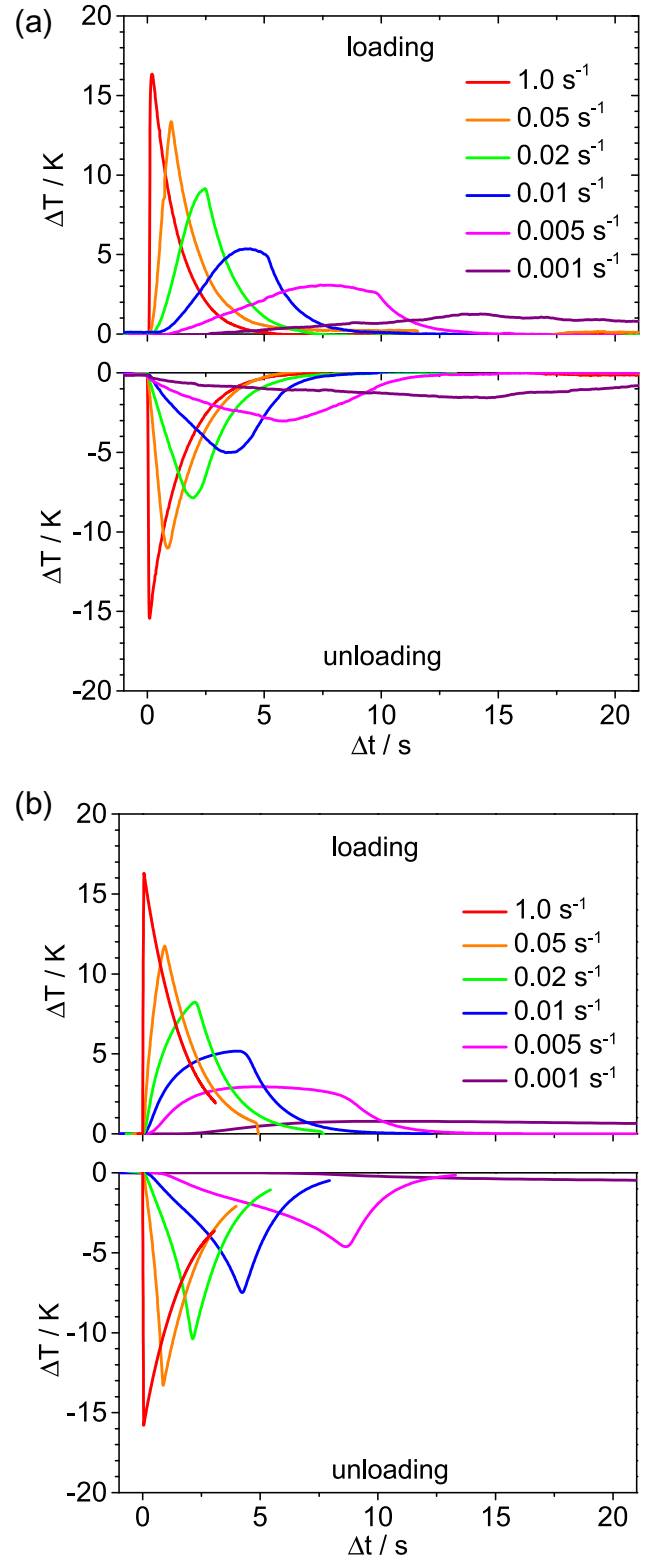


Fig. 9. (a) Evolution of maximum temperature during loading and minimum temperature during unloading of a TiNi film sample averaged over a representative area of 1 mm^2 . (b) Corresponding simulation characteristics.

critical stress for phase transformation of 500 MPa corresponds to a temperature shift of 55 K , which does not cover the full temperature range of the two-stage phase transformation.

The simulated strain-rate dependence of the peak temperatures is in good agreement with the experiment. In both cases, the adiabatic limit is reached at a rate of 0.2 s^{-1} . In the intermediate range between the quasi-static and adiabatic limit, the evolution of temperature is different upon loading and unloading due to the delayed onset of martensitic transformation compared to the instant onset of reverse transformation, causing an asymmetry in heat transfer over time. In this range, some deviation between experimental and simulated temperature change occurs upon unloading. This difference is attributed to imperfections and asymmetries of real samples, which are not considered in the model. As discussed in Section 6, the local stress distribution given by the details of boundary conditions determine the regions, where the phase transformation is initiated. These regions in turn affect the temperature evolution in adjacent regions. In the present case of unloading, the experimentally observed phase transformation initiates at the edges and the center of the sample (see Fig. 6). This causes a more complex temperature evolution compared to the simulation, and therefore some difference in strain-rate dependence (see Fig. 10). The observed small difference in the maximum temperature change upon loading and unloading in the adiabatic limit of 1 K is due to dissipation effects, which are not included in the simulation model.

Based on the experimental results on latent heat L and mechanical work ΔW , we estimate the material coefficient of performance $COP = L/\Delta W$. The mechanical work of a complete loading and unloading cycle is $\sim 6 \text{ J m}^{-3}$ (0.93 J g^{-1}) at high strain rates, yielding a COP of 7.7.

8. Discussion

The investigated TiNi films exhibit a large elastocaloric effect near the martensitic phase transformation of $|\Delta T| \approx 16 \text{ K}$ under adiabatic conditions. Nevertheless,

there is considerable room for improvement, as the accessible latent heat is only one-third of the latent heat of the full two-stage transformation of $\sim 20 \text{ J g}^{-1}$. This indicates that a maximum temperature change of 40 K or even beyond may be possible in the ultimate limit, which is in line with maximum reported values for TiNi bulk specimens [29]. However, reaching the adiabatic limit involves the application of large stress fields, which may lead to functional fatigue or even breakdown. This demands understanding the correlation between elastocaloric properties and functional fatigue. It has been shown that chemical doping of TiNi-based films is a promising route to suppress functional fatigue and to optimize hysteresis and thermal fatigue [11].

In the adiabatic limit, the observed difference between the maximum temperature change upon loading and unloading is rather small, $\sim 1 \text{ K}$. This result differs strongly from results on bulk specimens that reveal a significantly larger temperature change during loading compared to unloading, which has been attributed to frictional heating due to slip and other dissipating mechanisms [9]. Such dissipation effects seem to play a much smaller role in the investigated film specimens allowing for improved elastocaloric cooling performance compared to bulk.

A major reason for making use of film-based materials for elastocaloric cooling concerns the improved heat transfer due to high surface-to-volume ratios. Heat generation is determined by the strain rate $d\varepsilon/dt$. Adiabatic cooling performance is observed at a moderate strain rate of 0.2 s^{-1} , which corresponds to a time period of $\sim 250 \text{ ms}$ required for loading as well as unloading. Heat exchange with the environment by air convection and heat conduction through the sample fixation occurs with a time constant of $\sim 1.5 \text{ s}$, which is ~ 1 – 2 orders of magnitude shorter compared to the reported time constants for bulk specimens [9,30]. Moreover, heat exchange with a solid or liquid medium is expected to be even much faster, so that cycling rates of several Hertz seem to be feasible.

A common feature of martensitic phase transformation in film and foil specimens is the formation and evolution of Lüders-like strain bands [31,32]. This raises the question of how these local effects influence the temperature evolution during pseudoelastic loading and unloading. In our experiments, we observe a good correlation between the evolution of strain bands and temperature bands that form at the phase front of transforming and expanding regions. Formation of strain and temperature bands strongly depends on the mechanical and thermal boundary conditions. Sample fixation causes local stress accumulation as well as enhanced heat transfer between sample and support structures. Therefore, we observe band formation upon loading close to the sample fixation, where martensite formation is energetically preferred. Further evolution of local temperature profile correlates with the propagation of phase fronts. In addition, heat transfer effects and interaction between different temperature bands become important. With increasing load, phase fronts propagate from the sample fixation towards the sample center due to the

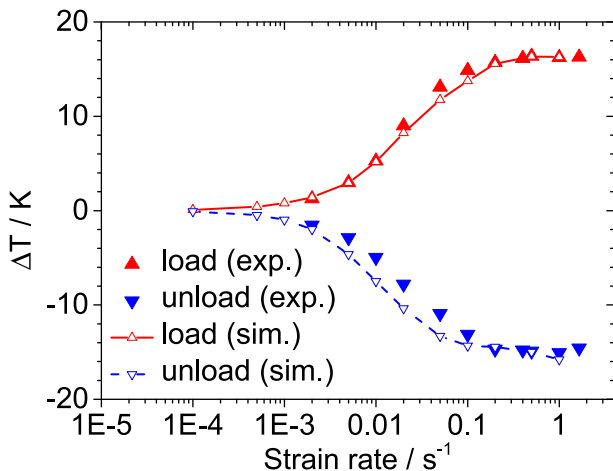


Fig. 10. Experimental and simulated strain-rate dependence of maximum temperature change upon loading and unloading. Minimum and maximum temperature values are taken from Fig. 9.

local interaction between neighboring transformed and untransformed regions. The evolution of strain and temperature bands upon unloading depends on the load history (see Fig. 6). In the case of incomplete martensitic transformation, phase fronts remain. Their propagation direction reverses during reverse transformation, resulting in the formation of undercooled temperature bands in the center of the sample. This process competes with the formation of austenite near the sample fixation, where enhanced heat transfer leads to reduced undercooling, and thus stabilization of austenite. In the experiment, both processes are observed. In addition, interaction between different temperature bands is observed, causing significant local overheating and undercooling. At high strain rates, the effects of self-heating/cooling due to the release/absorption of latent heat at the phase transformation front become important, which have a self-inhibiting effect on the transformation in adjacent sample regions. As a consequence, the formation of many transformation bands is favored [33].

Due to rapid heat transfer, the temperature bands quickly spread over $>100\text{ }\mu\text{m}$ within 100 ms. The temperature evolution on this time and length scale can be well described by the modified phenomenological simulation model. Both the time and spatially resolved averaged temperature profiles are well reproduced by the simulation results. Assuming complete phase transformation and symmetric boundary conditions, formation and propagation of temperature bands initiate from the sample fixation. This deviates from the temperature evolution under real boundary conditions that are generally not perfectly symmetric. The simulation results also reproduce the broadening and interaction of temperature bands as well as final temperature homogenization within $\sim 1\text{ s}$.

The COP of 7.7 deduced from the material characteristics hints at the large application potential of SMA film-based elastocaloric cooling. Concerning cooling applications, a useful figure of merit is the cooling power taking into account the constraints of the microcooling device. The presented results indicate that film-based materials enable complete thermodynamic cooling cycles within a fraction of a second if heat exchange is realized by direct contact to a solid/liquid medium. Thus, cooling power is expected to be superior for elastocaloric film cooling.

9. Conclusions

The spatially and time-resolved evolution of strain and temperature in magnetron-sputtered pseudoelastic TiNi films is investigated simultaneously during pseudoelastic loading and unloading with a frame rate of up to 100 Hz on a length scale down to $25\text{ }\mu\text{m}$. The heating/cooling time upon loading/unloading is essentially determined by the strain rate. Adiabatic conditions are reached at strain rates $>0.2\text{ s}^{-1}$. The rapid heat transfer enables the development of film-based elastocaloric cooling devices operating at cycling rates of several Hertz. The maximum temperature

decrease in adiabatic condition is $\sim -16\text{ K}$, which is limited by the accessible latent heat in the investigated test samples. As the maximum possible latent heat observed for TiNi-based alloys is of the order of 20 J g^{-1} , an increase by a factor of 2 seems to be possible.

The evolution of temperature profiles correlates with the local formation and propagation of Lüders-like strain bands. Within the observed time- and length-scale, the evolution of temperature profiles can be described by a phenomenological Tanaka-type model for phase transformation combined with a heat transfer model. By taking into account the boundary conditions of sample fixation and the local interaction between transformed and untransformed regions in the kinetics of martensitic phase fraction, the simulation model reproduces the formation and propagation of temperature bands as well as their interaction with good accuracy. Therefore, the presented simulation model is a useful tool for the engineering of elastocaloric microcooling devices. In general, the cooling performance of a SMA film-based cooling device is expected to be less affected by the local dynamics of strain and temperature bands compared to macroscopic SMA wire- and belt-like samples due to the rapid heat transfer.

The large temperature change, high material COP of 7.7 and the prospects of high cycling frequency are highly attractive for elastocaloric cooling and heat pumping. It is envisioned that SMA film devices may be grouped into large arrays to realize novel distributed cooling systems. In addition, SMA film-based cooling appears to be attractive for novel microcooling applications, where the ongoing miniaturization leads to severe thermal management problems. Well-known applications are in microelectronics, where the increasing power density of state-of-the-art processors and electronic components demand advanced cooling concepts. New emerging applications are, for instance, in biomedicine, e.g. local cooling of biological tissue and rapid blood cooling in microsurgery [34], and chemical analytics, e.g. temperature stabilization of lab-on-chip systems [35]. In these applications, conventional vapor compression is not suitable due to the need for relatively bulky compressors, while Peltier cooling is too inefficient. Nevertheless, the COP and cooling power of SMA-film-based cooling need to be demonstrated on the device level. Challenges in the development of optimum SMA film materials are to find a good compromise of suitable transformation temperatures, large temperature change and high reversibility. The fast heat exchange between the active material and the environment poses great demands on thermal insulation to minimize parasitic heat flows and losses [3]. From an engineering point of view, heat losses have to be kept at a minimum while providing fast heat transfer between the active material and heat source as well as heat sink. In order to achieve a high device COP, an efficient actuator is needed that is capable of providing the required driving force, while the mechanical work during pseudoelastic unloading needs to be recovered. In film-based devices, the required stress translates

to relatively small driving forces. The hysteresis width can be significantly reduced, e.g. by Cu addition, compared to the investigated binary TiNi film [11]. Thus, more work can be recovered during reverse transformation, which is beneficial to further increase the COP.

Acknowledgments

The authors gratefully acknowledge funding by the German Science Foundation (DFG) within the priority program SPP1599 (www.ferroiccooling.de). We would like to thank S. Seelecke for useful discussions on simulation.

References

- [1] Fähler S, Röbber UK, Kastner O, Eckert J, Eggeler G, Emmerich H, et al. *Adv Eng Mater* 2012;14(1–2):10. <http://dx.doi.org/10.1002/adem.201100178>.
- [2] Mañosa L, Planes A, Acet M. *J Mater Chem A* 2013;1:4925. <http://dx.doi.org/10.1039/c3ta01289a>.
- [3] Moya X, Kar-Narayan S, Mathur ND. *Nat Mater* 2014;13:439. <http://dx.doi.org/10.1038/NMAT3951>.
- [4] Mañosa L, Planes A, Vives E, Bonnot E, Romero R. *Funct Mater Lett* 2009;2(2):73.
- [5] Zimm C, Jastrab A, Sternberg A, Pecharsky VK, Gschneider KA, Osborne M, et al. *Adv Cryog Eng* 1998;43:1759.
- [6] Pecharsky VK, Gschneider KA. *Phys Rev Lett* 1997;78(32):4494.
- [7] Mischenko AS, Zhang Q, Scott JF, Whatmore RW, Mathur ND. *Science* 2006;311(5765):1270. <http://dx.doi.org/10.1126/science.1123811>.
- [8] Planes A, Manosa L. *Solid State Physics*, 55. New York: Academic Press; 2001.
- [9] Gschneider KA, Pecharsky VK, Tsokol AO. *Rep Prog Phys* 2005;68:1479.
- [10] Cui J, Wu Y, Muehlbauer J, Hwang Y, Radermacher R, Fackler S, et al. *App Phys Lett* 2012;101:073904. <http://dx.doi.org/10.1063/1.4746257>.
- [11] Lima de Miranda R, Zamponi C, Quandt E. *Adv Eng Mater* 2013;15(1–2):66. doi:10.1002/adem.201200197.
- [12] Bechtold C, Chluba C, Lima de Miranda R, Quandt E. *Appl Phys Lett* 2012;101:091903. <http://dx.doi.org/10.1063/1.4748307>.
- [13] Sutton MA, Mingqi C, Peters WH, Chao YJ, McNeill SR. *Image Vision Comput* 1986;99:124103.
- [14] Patoor E, Lagoudas DC, Entchev PB, Brinson LC, Gao X. *Mech Mater* 2006;38:391. <http://dx.doi.org/10.1016/j.mechmat.2005.05.027>.
- [15] Lagoudas DC, Entchev PB, Popov P, Patoor E, Brinson LC, Gao X. *Mech Mater* 2006;38:430. <http://dx.doi.org/10.1016/j.mechmat.2005.08.003>.
- [16] Brinson LC, Lammering R. *Int J Solids Struct* 1993;30(23):3261.
- [17] Auricchio F, Taylor RL. *Comput Meth Appl Mech Eng* 1997;143:175. [http://dx.doi.org/10.1016/S0045-7825\(96\)01147-4](http://dx.doi.org/10.1016/S0045-7825(96)01147-4).
- [18] Qidwai MA, Lagoudas DC. *Int J Numer Meth Eng* 2000;47:1123.
- [19] Peultier B, Ben Zineb T, Patoor E. *Mech Mater* 2006;38:510. <http://dx.doi.org/10.1016/j.mechmat.2005.05.026>.
- [20] Shaw JA. *Int J Solids Struct* 2002;39:1275. [http://dx.doi.org/10.1016/S0020-7683\(01\)00242-6](http://dx.doi.org/10.1016/S0020-7683(01)00242-6).
- [21] Grossmann C, Schaefer A, Wagner MFX. *Mater Sci Eng, A* 2010;527(4–5):1172. <http://dx.doi.org/10.1016/j.msea.2009.09.047>.
- [22] Tanaka K. *Res Mech* 1986;18:251.
- [23] Ikuta K, Shimizu H. In: *Proc MEMS 93*, Fort Lauderdale, USA, IEEE Catalog No. 0–7803-0957-2/93, p. 87–92.
- [24] Kohl M, Krevet B. *Mater Trans* 2002;43(5):251. <http://dx.doi.org/10.1117/12.484685>.
- [25] Krevet B, Pinneker V, Rhode M, Bechthold C, Quandt E, Kohl M. *Mater Sci Forum* 2013;738–739:287.
- [26] ASTM Standard E1269. Standard test method for determining specific heat capacity by differential scanning calorimetry. West Conshohocken, PA: ASTM International; 2011. doi: 10.1520/E1269-11.
- [27] He YJ, Sun QP. *Solid State Phenom* 2011;172–174:37. <http://dx.doi.org/10.4028/www.scientific.net/SSP.172-174.37>.
- [28] He YJ, Sun QP. *Int J Solids Struct* 2011;48:1688. <http://dx.doi.org/10.1016/j.ijsolstr.2011.02.017>.
- [29] Pieczyska EA, Gadaj SP, Nowacki WK, Tobushi H. *Exp Mech* 2006;46:531. <http://dx.doi.org/10.1007/s11340-006-8351-y>.
- [30] Pieczyska E. *J Mod Opt* 2010;57(18):1700. <http://dx.doi.org/10.1080/09500341003725748>.
- [31] Shaw JA, Kyriakides S. *Int J Plast* 1998;13(10):837.
- [32] Sittner P, Liu Y, Novak V. *J Mech Phys Solids* 2005;53:1719. <http://dx.doi.org/10.1016/j.jmps.2005.03.005>.
- [33] Zurbitu J, Kustov S, Zabaleta A, Cesari E. J Aurrekoetxea. In: Corneliu Cismasiu, editor. *Thermo-mechanical behaviour of NiTi at impact, shape memory alloys*. InTech; 2010. ISBN: 978-953-307-106-0.
- [34] Carmo JP, Silva MF, Ribeiro JF, Wolfenbuttel RF, Alpuim P, Rocha JG, et al. *Microsyst Technol* 2011;17:1283.
- [35] El-Ali J, Perch-Nielsen IR, Poulsen CR, Bang DD, Telleman P, Wolff A. *Sens Actuators, A* 2004;110:3.